

1 Reflection of linear internal tides from realistic topography: The

2 Tasman continental slope

3 JODY M. KLYMAK, *

School of Earth and Ocean Sciences and Department of Physics and Astronomy, University of Victoria, Victoria, Canada

4 Harper L. Simmons and Dmitry Braznikov

University of Alaska Fairbanks, Fairbanks, Alaska, USA

Samuel Kelly

Large Lakes Observatory and Department of Physics, University of Minnesota Duluth, Duluth, Minnesota

Jennifer A. MacKinnon, Matthew H. Alford, and Robert Pinkel

Scripps Institution of Oceanography, University of California, San Diego, La Jolla, California

Jonathan D. Nash

College of Ocean and Atmospheric Science, Oregon State University, Corvallis, Oregon

*Corresponding author address: Jody Klymak, University of Victoria, Victoria, BC, Canada

E-mail: jklymak@uvic.ca

ABSTRACT

9 The reflection of a low-mode internal tide on the Tasman continental slope is investigated
10 using simulations of realistic and simplified topographies. The slope is super-critical to the
11 internal tide, which should predict a large fraction of energy reflected. However, the response
12 to the slope is complicated by a number of factors: the incoming beam is confined in space;
13 it impacts the slope at an angle; there is a roughly cylindrical rise directly offshore of the
14 slope; and a leaky slope-mode wave is excited. These effects are isolated in simulations that
15 simplify the topography. In order to separate the incident from reflected signal, an incident
16 response without the reflector is subtracted from the total response to arrive at a reflected
17 signal. The real slope reflects approximately 65% of the mode-1 internal tide as mode-1, less
18 than two-dimensional linear calculations predict, due to the three-dimensional concavity of
19 the topography. It is also less than recent glider estimates, likely due to along-slope inho-
20 mogeneity. The inhomogeneity of the response comes from the Tasman Rise which diffracts
21 the incoming tidal beam into two beams, one focused downstream, and one diffracted to the
22 north. Along-slope inhomogeneity is enhanced by a partially trapped super-inertial slope
23 wave that propagates along the continental slope, locally removing energy from the internal
24 tide and re-radiating it further north. This wave is present even in a simplified straight-slope
25 topography, and its character can be predicted from linear resonance theory.

26 1. Introduction

27 Energy is lost from the surface tide when it interacts with topography and, in the deep
28 ocean, is largely redistributed as an internal tide. The fate of the internal tide is unclear, but
29 depends on the dominant wavelengths that are forced. Gentle topography that is subcritical
30 to the internal tide is likely dominated by higher vertical modes and is thought to break
31 via wave-wave interactions relatively close to the topography (i.e. Polzin 2009; St. Laurent
32 and Garrett 2002). Steeper supercritical topography, while exhibiting significant local
33 dissipation, tends to radiate a large fraction of the internal tide away from the topography
34 as low-mode waves (i.e. at Hawaii; Klymak et al. 2006; Carter et al. 2008). Given that a
35 significant fraction of the internal tide energy is generated at steep topography (Legg and
36 Klymak 2008), and that the distribution of the mixing it eventually drives has impacts
37 on understanding the distribution of ocean properties and the strength of the overturning
38 circulation (i.e. Melet et al. 2013), it is desirable to understand where and how the radiated
39 energy dissipates.

40 One candidate sink for the low-mode internal tide is scattering and dissipation from
41 continental slopes. These slopes are known to be hotspots of turbulent mixing from the few
42 observational studies to date (Nash et al. 2007; Klymak et al. 2011; Martini et al. 2013).
43 However, these studies have also demonstrated some of the difficulties in tracking internal tide
44 energy on these slopes. Net internal-tide fluxes are relatively straight forward to measure,
45 but ideally we would like to separate the incident and reflected fluxes if a parameterization of
46 turbulence on the slope is to be made, since the incident fluxes are what drive the turbulence.
47 The reflectivity of a continental slope is the ratio of the energy flux convergence divided by

48 the total incident flux:

$$R = \frac{F_{out}}{F_{in}}, \quad (1)$$

49 where F is depth-integrated for a two-dimensional budget or line-integrated for a three-
50 dimensional one. Even simple two-dimensional linear models of reflection indicate that de-
51 termining the reflectivity will be challenging, with reflection co-efficients strongly depending
52 on the modal content and phases of the incident internal tides (Klymak et al. 2011) and the
53 local surface tide (Kelly and Nash 2010). These linear models have been used globally to es-
54 timate reflection co-efficients for the mode-1 tides on realistic continental slope bathymetries,
55 (Kelly et al. 2013b,a), but these calculations assume the incoming tide is known, and that
56 the topography is relatively homogenous over a distance similar to the mode-1 horizontal
57 wavelength.

58 Determining the incident flux, F_{in} , from field data, and even from a numerical model
59 with sufficient complexity, is not trivial. In two dimensions, or with simple plane wave
60 geometries, it is straight forward to fit incident and reflected plane waves to recover the
61 desired reflection co-efficient (figure 1a). In the real ocean, even if tidal signals can be
62 separated from confounding influences, internal tides are often spatially inhomogeneous,
63 and form lateral “beams” (in x-y; Rainville et al. 2010) that make plane wave fits difficult
64 from a finite array of moorings; for instance a mooring array could be located more in the
65 incoming beam than in the reflected, leading to an exaggeration of the computed energy
66 convergence (figure 1b). Plane-wave fits to satellite altimetry tracks are promising, but will
67 also suffer from a lack of fidelity if the internal tides are inhomogeneous on the scale of the
68 plane wave fits (Zhao and Alford 2009). In the model, high resolution temporal and spatial

69 information makes it possible to separate signals spectrally according to their direction of
70 propagation (i.e. using a Hilbert transform, Mercier et al. 2008), but this method works best
71 if there are no boundaries and the signals at the edges of the model domain can be tapered
72 to reduce Gibbs ringing, neither of which are applicable in the nearfield of a continental
73 slope.

74 The region considered here is the Tasman continental slope, the focus of a concentrated
75 internal tide field experiment. As preliminary work, it has been sampled continuously by
76 gliders for a number of months in 2012 and 2013 (Johnston et al. 2015). The gliders were
77 flown to form and antenna over which internal plane-wave fits were made. These efforts show
78 a standing wave pattern, with amplitudes and phases as one would expect for internal waves
79 incident on the slope from the southeast where internal tides are expected to be generated
80 from the Macquarie Ridge (figure 2a). The amplitudes of the interfering waves were such
81 that the reflectivity is predicted to be high on this slope, with estimates of 0.7 to 1.0 from
82 the arrays (Johnston et al. 2015). The gliders also picked up a 100-km wavelength wave
83 propagating along slope towards the north, a finding we isolate and discuss below.

84 Here we run numerical simulations that are meant to represent a mode-1 internal M_2
85 tide incident on the Tasman Slope, east of Tasmania. The simulations are only forced by
86 the incident internal tide, and there is no local forcing, allowing the reflection signal to be
87 isolated. After discussing the model setup section 2, we briefly consider the response this
88 forcing has on the slope section 3 and compute and energy budget of the complete response.
89 In order to separate the physics of the reflection, we then simplify the geometry section 4,
90 both geometrically, and by removing parts of the topography. This technique allows us to
91 separate incident and reflected signals from the total response without appeal to plane wave

92 fits. We end with a discussion of the results (section 5) where we note the applicability of two-
93 dimensional reflection models and discuss the leaky slope waves evident in the simulations.
94 We conclude with a summary (section 6).

95 2. Model setup

96 a. Basics

97 The numerical model used here is the MITGCM (Marshall et al. 1997), visualized using
98 the Python scientific stack (Hunter 2007; van der Walt et al. 2011). The setup is very similar
99 to Buijsman et al. (2014), with the model run in hydrostatic mode, background (isotropic)
100 diffusivities and viscosities of $10^{-5} \text{ m}^2 \text{ s}^{-1}$, and enhanced diffusivity and viscosity in regions
101 of temporarily unstable stratification (Klymak and Legg 2010). A second-order flux-limiting
102 temperature advection scheme is used which results in some numerical dissipation and dif-
103 fusion. Sensitivity tests were run with weaker forcing, and the fraction of energy dissipated
104 in the model did not change, indicating that the dissipation highlighted below is dominated
105 by numerical dissipation due to the lack of lateral resolution (1 km) rather than explicit
106 viscosities. Dissipation is not the main focus of this paper, and finer resolutions have been
107 used for more focused efforts dealing with turbulence on the slope (in preparation). These
108 simulations are therefore the most “linear” that the resolution will allow.

109 Topography is from a data set that combines Smith and Sandwell (1997) and multibeam
110 data from Australian surveys (Whiteway 2009) (figure 2b). For this paper, we use a Cartesian
111 co-ordinate system centered at 44 S, 148 E, with y pointing 12 degrees east of geographic

112 north (magenta lines, figure 2). This co-ordinate system is close to cross-slope in the x-
113 direction, and is used for conceptual convenience. The simulations are run on a f-plane
114 ($f = -10^{-4} \text{ s}^{-1}$).

115 A 1-km lateral resolution is used along the continental slope (figure 3a, smallest inset
116 green box). Resolution is expanded by 3.5% per grid cell beyond the 1km-resolution region,
117 to a maximum of 5 km in the second largest inset box (figure 3a); this keeps the resolution
118 over the Tasman Rise and the rest of the continental slope at least 5 km. Further out, the
119 grid spacing is again increased at 3.5% per grid cell until a maximum grid cell size of 10 km
120 is reached.

121 Vertical resolution is approximately stretched so $dz \sim 1/N$, where $N^2(z) = -\frac{g}{\rho_0} \frac{d\rho}{dz}$ is the
122 vertical stratification. 200 vertical grid cells are used for these simulations. The vertical
123 stratification is from the World Ocean Atlas for the Tasman Sea just offshore of Tasmania
124 (Boyer et al. 2013), and is assumed laterally constant in the domain. This precludes any
125 mesoscale effects, which are believed to be important in this area, and are the subject of
126 future work.

127 *b. Forcing*

128 To simplify the generation problem we apply an analytical forcing to our model. This
129 is composed of two line sources at approximately the location of the Macquarie Ridge (fig-
130 ure 3a). The initial conditions and the southern and eastern boundaries of the model were
131 set with this forcing. The forcing is similar to that suggested by Rainville et al. (2010),
132 except instead of a single point source placed a distance R from the line source, the line

₁₃₃ source is digitized as a number of discrete point sources and their response in the domain
₁₃₄ summed. The mode-1 pressure anomaly is given by:

$$p'(x, y, t) = \sum_{i=1}^N a_i \exp(j(|k_t|r_i - \omega t)) \quad (2)$$

₁₃₅ where $r_i = \sqrt{(x - x_i)^2 + (y - y_i)^2}$ is the distance to the source, and $|k_t|$ is the absolute value
₁₃₆ of the mode-1 wavenumber:

$$k_t = \frac{(\omega^2 - f^2)^{1/2}}{c_e} \quad (3)$$

₁₃₇ where ω is the frequency of the tide, f is the Coriolis frequency, and c_e is the eigenspeed of
₁₃₈ the vertical mode equation:

$$\frac{d}{dz} \left(\frac{1}{N^2} \frac{d\psi}{dz} \right) + \frac{1}{c_e^2} \psi(z) = 0. \quad (4)$$

₁₃₉ Here $\psi(z)$ is the eigenfunction that sets the shape of the vertical mode, and the bound-
₁₄₀ ary conditions are $d\psi/dz = 0$ at $z = 0$ and $z = -H$, where H is the water depth. For
₁₄₁ convenience, we normalize $\psi_m(z)$ so that

$$\int_{-H}^0 \psi_m(z) \psi_n(z) dz = \delta_{mn}. \quad (5)$$

₁₄₂ Horizontal velocities can be linearly decomposed by these shapes, as can the pressure signal.
₁₄₃ To compute the wavefield, the horizontal velocity components are derived from the in-
₁₄₄ ternal wave consistency relations:

$$u(x, y, t) = \sum_{i=1}^N \frac{k_x \omega + j k_y f}{\omega^2 - f^2} \frac{p'_i}{\rho} \quad (6)$$

$$v(x, y, t) = \sum_{i=1}^N \frac{k_y \omega - j k_x f}{\omega^2 - f^2} \frac{p'_i}{\rho} \quad (7)$$

₁₄₅ where $k_x = k_t \cos(\theta_i)$ and $k_y = k_t \sin(\theta_i)$ are calculated from the angle to each element of the
₁₄₆ line sources $\theta_i = \arctan((y - y_i)/(x - x_i))$.

147 The resulting incoming wavefield (figure 3a) has a beam of energy flux that radiates
148 northwest, and is relatively tightly focused. The interference pattern creates a null to the
149 south and north, and a secondary beam that radiates due west. This schematic agrees with
150 more realistic regional tidal models (H. Simmons, in preparation), and the amplitude of the
151 beam was tuned to give approximately 2 kW m^{-1} incident at Tasmania. Note this is less
152 than estimates from altimetry and numerical simulations, and is purposely low to keep the
153 runs as “linear” as possible. The initial condition is applied uniformly through the domain,
154 regardless of bathymetry, so there are some start-up transients as the proper baroclinic flow
155 develops.

156 The northern and western boundaries are sponges where the velocity is slowly dropped
157 to zero and the stratification relaxed to the initial stratification (figure 3a, green rectangles).
158 Our main focus is the area from $y=0$ to 400 km, so the boundaries are sufficiently far that
159 small residual reflections do not affect the response.

160 The ideal response off the Tasman topography would be as a plane-wave reflection from
161 a wall at $x = 0$ km (i.e. Johnston et al. 2015). Here we have a relatively confined beam,
162 but we can make a start by considering the reflection the beam from a wall at $x = 0$ km for
163 $y > 0$ km (figure 3b,c) using the method of images with identical line sources mirrored about
164 the y-axis, and their phase shifted by 180 deg. The reflection pattern that sets up is not
165 entirely regular, but has some straight-forward features. The incoming beam impacts the
166 wall at approximately 30 deg. The horizontal wavelength of an M_2 internal tide is 178 km,
167 so the standing wave in the x-direction will have a wavelength $178/\cos(30) \approx 200$ km and
168 in the y-direction will have a wavelength of approximately 350 km. These spatial scales
169 are readily apparent in the analytical forcing despite the non-plane-wave character of the

₁₇₀ idealized forcing (figure 3c). Note that the standing energy flux (figure 3b) has peaks and
₁₇₁ nulls in absolute value, with the peaks having large flux to the north. The peaks are every
₁₇₂ half cross-slope wavelength (i.e. 100 km). The nulls have weak southward energy flux (though
₁₇₃ it is difficult to discern from the subsampled arrows in the plot).

₁₇₄ 3. Realistic model simulation

₁₇₅ The response of the forcing in the most real bathymetry motivates the more idealized
₁₇₆ experiments that follow. From the initial forcing (figure 4a), a complex wavefield develops
₁₇₇ with clear scattering from the Tasman Rise, the shelf, and numerous small inhomogeneities
₁₇₈ on the sea floor (figure 4b–d). Looking along slope, the phase of the velocity signal can
₁₇₉ be seen changing approximately every 200 km, and it changes approximately every 100 km
₁₈₀ offshelf similar to what we expect from an oblique standing wave (compare figure 4h to
₁₈₁ figure 3b). However the pattern is complicated, not lining up in the north-south direction
₁₈₂ and inhomogeneities in the energy that are not accounted for by a simple two-wave model.

₁₈₃ A time-averaged energy balance is performed online in the model using the terms outlined
₁₈₄ in Kang and Fringer (2012); Kang (2011). The energy balance vertically integrated can be
₁₈₅ schematized as:

$$\frac{dE_{bc}}{dt} = -\nabla_H \cdot \mathbf{F}_{bc} + \text{Conversion} - \text{Dissipation}. \quad (8)$$

₁₈₆ where E_{bc} is the depth-integrated baroclinic energy density, \mathbf{F}_{bc} is the depth integrated energy
₁₈₇ flux, including both the pressure work term and the non-linear advection of energy (which
₁₈₈ is small in our runs). All quantities are averaged over an M_2 tidal period. “Conversion”

is a complex term representing transfer from barotropic motions to baroclinic (Kang 2011, eq. 5.102) and includes the barotropic heaving of the water column, the density anomaly, and a non-linear horizontal advection term. These non-linear terms can be non-trivial in real bathymetry (Buijsman et al. 2014). The conversion term is positive if the barotropic tide loses energy and the baroclinic tide gains energy. “Dissipation” is computed here as the residual, and includes dissipation due to explicit viscosity, numerical dissipation, and bottom drag.

Of note in the energy calculation is that the largest local term in the energy budget is an alternating pattern of barotropic-baroclinic conversion at the shelf break balanced by baroclinic flux convergences and divergences (figure 5). The importance of the barotropic-baroclinic term can also be seen by considering the x-integral of the energy budget from $x = -50$ km to $+100$ km (figure 6). Recall that the simulations have no barotropic forcing. This coupling is catalyzed by a start-up transient hitting the slope with the incoming internal tide beam, and continues throughout the simulation, and is a leaky super-inertial slope wave (see section 5).

The time series of the energy terms integrated along the slope demonstrates that the barotropic-to-baroclinic term is relatively small when averaged, with a small loss of energy from the baroclinic tide to the barotropic in the integral region (figure 6b). The model is largely in a steady state by tidal cycle 15, with some residual oscillations in dE/dt and the flux convergence. The large-scale baroclinic energy changes do not change the dissipation residual very much, which is relatively constant after 5 tidal cycles. To put the 50 MW of dissipation into context, the initial energy that comes in the east and south sides of this analysis box in the initial conditions is 315 MW, so the model is dissipating about 17% of

the incoming energy. However, note that the dissipation is not the focus of these model runs nor of this paper. The forcing here is approximately a factor 3 lower than the real forcing, so its likely the fraction of dissipation at this site is higher if real forcing is used.

The majority of the energy budget is in the first vertical mode (figure 6c). Net fluxes in the region directly offshore of the shelf break ($0 < x < 80$ km, and $0 < y < 400$ km) are composed of substantial mode-1 energy converging on the slope (95 MW net), and some reflected energy escaping in higher modes (28.3 MW, mostly in modes 2–4). The 95 MW net flux is made up of the incoming and reflected mode-1 energy, and separating those terms is the subject of the next section. There is some incoming higher-mode energy as well due to scattering from the Tasman Rise, but as we will also show below, this is minor. The spatial pattern (not shown) of the mode conversion at the continental slope indicates hot-spots for conversion. Modes 2 and 4 have a hotspot of conversion near $y = 250$ km, and mode 3 at $y = 325$ km.

4. Simplified geometries

To help tease apart the effects of the Tasman Rise and the non-uniform slope, we carry out a few simplified experiments (figure 7; figure 8). The **REAL** case is the one discussed above (figure 8f). The **NO TOPO** case has no topography at all (figure 8a), just the beam being forced at the south and east boundaries and (mostly) absorbed at the west and north. **RISE** was run with the real bathymetry west of $x = 70$ km (figure 8e). Three idealized geometries simplify the physics even more: the **SHELF** case has a supercritical two-dimensional continental slope running north from $y = 0$ km (figure 8d). **ROUND RISE** is a 1700-m tall

233 cylinder-shaped bump with radius of 50 km centered at approximately the same location as
 234 the Tasman Rise, with no shelf to the west (figure 8b). The simplified slope and the rise are
 235 both used in the SHELF/RISE case (figure 8c).

236 *a. Shelf-only configuration*

237 The simplest topography is the SHELF configuration (figure 8d). Here we have a response
 238 that is quite similar to the analytical response calculated above (figure 3b). The only differ-
 239 ence between these two cases is the narrow shelf west of $x = 0$ km and the slight slope to
 240 the continental slope. The interference pattern between the incoming wave and the reflected
 241 wave is clear in this plot, with the same characteristic length scales as above, and a slight
 242 bending of the response due to the radial spreading of the beam.

243 The goal of this paper is to determine the amount of reflectivity of the continental slope.
 244 This is a hard number to determine in a complicated geometry, and naturally depends on
 245 the region of integration. For the SHELF configuration the situation is relatively simple, and
 246 we use it to illustrate the numerical technique used below. The signal in the full simulation
 247 is assumed to consist of an “incoming” signal and a reflected signal, so we can decompose
 248 the east-west velocity amplitude of the first vertical mode (for example) as:

$$u_1^t(x, y) = u_1^i + u_1^r \quad (9)$$

$$v_1^t(x, y) = v_1^i + v_1^r \quad (10)$$

$$p_1^t(x, y) = p_1^i + p_1^r \quad (11)$$

249 where u_1^t is the complex amplitude of the M_2 , mode-1 east-west velocity of the simulation
 250 with the reflection, u_1^i of the incoming signal, and u_1^r of the reflected signal. We assume for

251 this example that the incoming signal u_1^i is given by the NO TOPO simulation, and u_1^t is
 252 from the SHELF simulation. The reflected signal u_1^r is simply the difference of these two.
 253 This method has been used by Hall et al. (2013) for a two dimensional flow. Here it is an
 254 absolute necessity because of the complicated three-dimensional topography.

255 In order to compute and energy budget, we consider that the energy fluxes are calculated
 256 from the decomposed signals as:

$$F_{u1}^t = u_1^t p_1^t \quad (12)$$

$$= \underbrace{u_1^i p_1^i}_{\text{Incoming}} + \underbrace{u_1^r p_1^r}_{\text{Reflected}} + \underbrace{u_1^i p_1^r + u_1^r p_1^i}_{\text{Cross Terms}} \quad (13)$$

$$F_{v1}^t = v_1^t p_1^t \quad (14)$$

$$= \underbrace{v_1^i p_1^i}_{\text{Incoming}} + \underbrace{v_1^r p_1^r}_{\text{Reflected}} + \underbrace{v_1^i p_1^r + v_1^r p_1^i}_{\text{Cross Terms}} \quad (15)$$

257 The cross terms are not negligible for any realistic forcing, and indeed give rise to the
 258 interference patterns seen above (Nash et al. 2004; Martini et al. 2007).

259 The “total” response (figure 9d) consists of the incoming response (figure 9a), and the
 260 “reflected” signal (figure 9b), and substantial cross-terms (figure 9c). The cross terms are
 261 mostly perpendicular to the direction of reflection (i.e. parallel to the slope) and alternately
 262 flux energy to the north and south every half cross-slope wavelength. Combined, these three
 263 components give the “total” flux with net fluxes to the north in alternating peaks every full
 264 offslope wavelength.

265 The reflected response (figure 9b) shows approximately what we would expect with energy
 266 being radiated to the north-east. There is some concentration of this energy at $y \approx 75\text{km}$,
 267 and $y \approx 225\text{km}$ because of coupling with a partially trapped slope wave. This coupling
 268 causes a redistribution of the reflected energy, focusing it approximately every along-slope

269 wavelength of the slope wave (we show in section 5 that this wavelength changes as the slope
270 geometry changes).

271 Performing this analysis for the lowest 10 modes, we arrive at an energy budget for the
272 slope in the green box in the figures ($0 < y < 400$ km, and $x < 80$ km; figure 9, inset
273 budgets). Note that we assume the flux through $x = 0$ is zero. With this calculation, we see
274 that 408 MW is incident on the slope in mode-1. There is also a net flux of 50 MW into this
275 region from the cross terms. This is a redistribution of energy from north of our box into
276 the box. There is a net convergence of this cross-term energy because there is dissipation in
277 the box; in a purely inviscid solution this term should balance to zero over a closed box. If
278 we extend the integration further north, the cross-term flux drops to zero.

279 Most of the incoming energy reflects back out of the box (figure 9b), with the bulk
280 remaining in mode 1, and some scattering to higher modes. This scattered energy radiates
281 to the north east (not shown). The mode-1 reflection is affected by the slope wave that
282 transfers energy to and from the barotropic tide along the slope, resulting in nulls and peaks
283 in the mode-1 reflection.

284 *b. Tasman Rise only*

285 The Tasman Rise has a profound effect on the energy that impacts the continental slope
286 (figure 8e and f). The incoming beam is almost 500 km wide at $x = 0$ if there is no
287 Tasman Rise, but breaks into three narrower beams when there is a Tasman Rise (figure 8e).
288 Upstream of the rise, the effect is somewhat less energy propagating westward, with an
289 interference pattern towards the east indicating some back reflection.

290 This pattern can be explained in terms of diffraction of the internal tide beam from a
291 deep obstacle (i.e. Johnston and Merrifield 2003). There is a down-wave concentration of
292 energy along the seamount's axis, a null, and sidelobes to the north and south. In this case,
293 the incident beam is of comparable size to the obstacle, leading to an asymmetry, and a
294 stronger lobe to the north than south.

295 Most of the response due to the Tasman Rise can be modeled simply as a cylindrical
296 obstacle in the beam (figure 8b and c). Here our obstacle is 1800 m high in 5000 m of
297 water, and has a radius of 50 km (figure 7). This captures most of the features of the actual
298 Tasman Rise, despite not having a shallow spire in the center and being slightly smaller than
299 the real Rise. The differences make the simplified response have weaker nulls and the whole
300 response is directed a bit further north than the real Rise. Adding the shelf (figure 8c) yields
301 a response that bears substantial similarity to the REAL forcing case.

302 Decomposing into an incoming and reflected signal (figure 10) demonstrates the effect
303 of the Tasman Rise on the response. Less energy is incident on the control volume, largely
304 because the diffraction redirects some of that energy to the north of $y = 400$ km. There is a
305 strong reflection of energy where the main diffraction lobe reflects from the slope (figure 10b),
306 and a smaller maximum just to the north ($y = 250$ km) due to the along-slope wave that
307 is strummed. There is a reflection further north where the northern lobe of the diffraction
308 pattern reflects.

309 The incoming energy has some more high-mode content due to scattering at the cylindri-
310 cal rise (figure 10a), though it is still 95% mode-1. The reflection is almost 80% mode-1, with
311 some scattering to higher modes. The net flux shows approximately 15% of the incoming
312 energy is dissipated at the shelf.

313 *c. Real Case*

314 The REAL forcing is similar, if more complex (figure 11). The simulation using the
315 bathymetry in the RISE ONLY case (figure 8e) is used as the “Incoming” energy flux, and
316 the REAL (figure 8f) case is the “Total”. Compared to the cylindrical rise, the real Tasman
317 Rise creates a sharper diffraction pattern, and more back reflection. However, the REAL
318 simulation has many of the same features as the SHELF/RISE simulation (figure 8c).

319 Slightly less incoming energy passes into the control volume (figure 11a) because the
320 diffraction by the real Tasman Rise is sharper than the cylindrical rise. As for the cylindrical
321 rise case, there is some incoming higher mode energy due to forward scattering, though again
322 over 95% is mode-1. Reflection is concentrated near $y = 125$ km and $y = 450$ km, associated
323 with the diffraction nodes, with about 85% in mode 1 (figure 11b). Dissipation is less than
324 25% of the incoming energy (figure 11d).

325 5. Discussion

326 *a. Estimating reflection co-efficients*

327 A major goal of this effort is estimating the fraction of incoming tide that is reflected by
328 the Tasman continental slope to come up with a reflectivity co-efficient. Here we discriminate
329 between the mode-1 reflection, $R_1 = F_{ref,1}/F_{in,1}$, and the total reflection into all the modes,
330 $R_T = F_{ref}/F_{in}$. Evaluating these co-efficients is less straightforward than it may sound
331 because it is difficult to separate the incoming from reflected signal in complicated geometry,
332 even in a fully resolved numerical model, let alone in observations. Above, we used an

integrated measure, comparing the incoming flux from a model with no continental slope to one with a continental slope and integrating the fluxes over a control volume from $y = 0$ to 400 km. This control volume was an arbitrary choice, but yielded reflectivities of mode -1 internal tide $R_1 = 0.65$ and the total internal tide of $R_T = 0.76$ (figure 11).

Determining reflectivity from a mooring array is significantly complicated by three-dimensionality and along slope variability. From the mooring array in figure 11, the reflectivity is $R_1 = 0.6/1.3 = 0.46$, a significant under-estimate. The reason for this should be relatively clear from looking at figure 11a,b; the mooring array nicely captures the northward diffracted ray, but catches some of the reflected pattern from the main beam to the south. There are significant interferences in the reflected patterns (figure 11b) because the reflected pattern is a complicated superposition of the cylindrically spreading reflections along the slope.

Determining the reflectivity as a function of along-slope direction y is difficult. Simply lining up the onslope fluxes does not yield useful results because the reflection from any given point on the slope radiates cylindrically, and it is necessary to integrate over volumes. Here we take the same approach as used in the previous section (i.e. figure 11), but integrate over smaller control volumes (80 km in y) to see the reflectivity as a function of y (figure 12a,b). The incoming flux every 80 km shows the diffracted beam pattern with a maximum net incoming flux at $y = 120$ km (figure 12a, red line) and a secondary peak to the north at about 440 km. The net reflectivity from these boxes ranges from 0.8 to a low of almost zero at $y = 280$ km (figure 12b, solid blue line). Note an uncertainty in the flux decomposition associated with the flux in the cross terms (figure 12a, purple line). This term does not balance to zero, and forms a significant part of the energy budget over such small control

356 volumes. It cannot be uniquely decomposed into either the incoming or reflected energy
357 terms, so remains as an uncertainty.

358 In two-dimensions, the fraction of the tide reflected into mode 1 (and higher) can be
359 predicted from linear theory using the method described by Kelly et al. (2013a) of matching
360 Laplacian tidal solutions at discrete steps on a discretized topography. If the tide is obliquely
361 incident on the slope, there can be substantial differences in the reflected tide (Kelly et al.
362 2013b). If we run these solutions for the Tasman Slope with an incident angle of 30 degrees,
363 the reflectivity into mode-1, R_1 is similar to the numerical simulation (figure 12b, thick black
364 line). The predicted reflectivity is greater for most of the ridge, but the null at $y = 250$ km
365 is captured.

366 The REAL simulation has a mode-1 reflectivity of $R_1 = 0.65$. A naive average of the
367 reflectivity from the linear model between $y = 0$ and 400 km yields $\langle R_1 \rangle = 0.71$. However,
368 that does not take into account the varying strength of the incoming diffracted beam, which
369 is stronger where the reflectivity is higher. Weighting by the incoming beam strength, then
370 the reflectivity averages $\langle R_1 \rangle_{beam} = 0.8$, and is substantially larger than in the numerical
371 simulations.

372 An attempt has been made to estimate reflectivity from this site from autonomous gliders
373 surveys (Johnston et al. 2015). First, the gliders saw a substantial concentration of energy
374 shoreward of the Tasman Rise. This is a feature of the model, and clearly explained by the
375 diffraction of energy by the Tasman Rise (figure 11).

376 For the region in the lee of the Tasman Rise, Johnston et al. (2015) estimate a reflectivity
377 of the mode-1 internal tide of between 0.8 to 1.0 by fitting plane waves to the velocity and
378 displacement amplitudes and phases. If we confine our incoming versus outgoing energy

379 budget to the region $80 \text{ km} < y < 200 \text{ km}$, representative of their *Spray 56* deployment, we
380 calculate a reflectivity of 0.7, which is lower than their lowest estimate of 0.8, and much lower
381 than their high estimate of 1.0. A second deployment, *Spray 55*, covered more of the slope
382 (up to $y = 300 \text{ km}$). In this domain, they estimate a reflectivity of 0.6. This is in agreement
383 with the numerical simulation, which achieves the same result from $0 \text{ km} < y < 300 \text{ km}$.

384 The directions of wave propagation fit from the glider data is not in agreement with
385 the model. The fits to the *Spray 55* data show incoming energy at between 125 and 145
386 degrees, which is similar to the model. However the reflection is slightly south of due east
387 (0 to -30 degrees geographic), whereas the numerical model is definitely to the northeast
388 far from shore. An explanation is evident from close inspection of figure 11b between the
389 Tasman Rise and the continental slope where the glider spent the most time. At this location
390 the off-shore energy flux is almost exactly in the x-direction, (-12 degrees geographic), in
391 agreement with the glider observations.

392 Finally, one of the gliders (*Spray 56*) picked out a northward propagating disturbance
393 along the continental slope with wavelength of 100 km. This wavelength matches the wave-
394 length of the slope wave seen in the real simulations (figure 5a,b). Interestingly, they only
395 pick this wavelength out in vertical displacement data, not in velocity.

396 *b. Slope wave importance and dynamics*

397 The structure of the barotropic-to-baroclinic conversion on the slope is an intriguing fea-
398 ture of these simulations, and appears in regional simulations (Simmons, in prep) and the
399 glider data (Johnston et al. 2015). Here, it shows up most clearly in the SHELF simulations

400 because of the simplified bathymetry. However, it is also clear in the REAL simulation (fig-
401 ure 5a). This slope wave redistributes energy in the reflected baroclinic response (figure 9),
402 taking a relatively homogenous incoming energy source and focusing the reflection every 200
403 km or so along slope.

404 This wave is a slope mode that is strummed by the incident internal tide at the “corner” of
405 the topography ($x = 0, y = 0$); a long slope without the corner does not excite this wave, nor
406 does an internal tide coming directly from the east and hitting the topography at a normal
407 angle. The along-slope wavelength is independent of the incident along-slope wavelength
408 in the open water (tested by changing the angle of the incident tide; not shown), and is a
409 robust feature of the slope shape. A sensitivity experiment that varied the continental slope
410 widths demonstrates that narrower slopes strum longer along-slope waves (figure 13).

411 These waves are super-inertial and are an example of partially trapped slope waves (Dale
412 and Sherwin 1996; Dale et al. 2001). We compare the wavelength of the slope waves (fig-
413 ure 14, thick lines) to the empirical modes predicted from linear theory (Dale et al. 2001).
414 The procedure solves for the response of the flow in the coastal bathymetry due to forcing
415 with varying along-slope wavelengths. Resonant along-slope wavelengths lead to a much
416 stronger response (Appendix and figure 14, thin lines). The along-slope wavelength of the
417 resonant modes in the linear calculation agree quite well with the wavelengths of the fully
418 non-linear solutions. Narrower continental slopes yield longer along-slope wavelengths, and
419 the spatial modes that correspond to the peaks are similar to deep-ocean mode-1 off the
420 slope.

421 The slope wave is an important term in the local energy budget when compared the
422 incoming and reflected energy fluxes (figure 15). The incoming energy peaks at 1.2 kW/m,

423 and the reflected energy is of a similar magnitude but with oscillations at twice the wave-
424 length of the slope wave. The integrated barotropic-baroclinic conversion is as high as 0.4
425 kW/m-coastline, and leads to 0.4 kW/m peak-to-peak oscillation in the reflected energy
426 (its not 0.8 kW/m peak-to-peak because the reflected energy spreads spherically by 40 km,
427 where the reflected flux is evaluated, figure 9). This turns even a relatively straight slope
428 into a series of internal tide absorbers and radiators, leading to 100-km scale inhomogeneity
429 in the reflected internal tide.

430 6. Summary

431 A mode-1 internal tide was launched at a variety of topographies representing the Tasma-
432 nian continental slope. The goal was to determine the “reflectivity” of this slope, in terms of
433 the modal content of the reflected energy and the local dissipation. The latter is somewhat
434 suspect in this model because of crude lateral resolution, but the REAL simulation indicated
435 that 21% of the incoming energy was dissipated, and 65% was reflected as mode-1 energy.
436 The incoming internal tide flux used here was weak compared to the flux modeled and in-
437 ferred from altimetry in the Tasman Sea, so we expect the dissipation in more realistically
438 forced models to increase.

439 Despite a simple incoming internal tide that is linear, semi-diurnal, and mode-1, we have
440 found a rich and complex response of the topography when the remote wave impacts the
441 topography. The response can be characterized as follows:

- 442 • diffraction of the beam by the Tasman Rise,

- 443 • oblique reflection from the continental slope,
444 • and a leaky slope wave response that redistributes reflected internal energy along-slope.

445 Of these, perhaps only the second effect was expected before carrying out the simulations.
446 However, as we saw above, even the reflection problem is significantly complicated in the
447 presence of three-dimensionality.

448 Diffraction around underwater topography should have been expected, however, the rel-
449 ative depth of the obstacle makes it surprising that the effect is so strong. The fact that
450 the lateral width of the Tasman Rise is close to the wavelength of the incoming internal
451 tide makes predicting the diffraction pattern difficult. Baines (2007) considers generation of
452 internal tides at seamounts, but does not deal with scattering and diffraction. The problem
453 is similar to electromagnetic waves passing through a wire, but a linear response for that
454 problem is not trivial to compute (i.e. Bonod et al. 2005), and still does not have a confined
455 vertical mode structure as we find in the internal wave problem.

456 The excitation of slope waves has been explored by Dale et al. (2001). It has an important
457 effect on the redistribution of energy along slope. The redistribution affects where high
458 dissipation is found in the model (figure 5), and adds more inhomogeneity to the reflected
459 internal tide.

460 The complexity grows if other real-world influences are to be accounted for. The East
461 Australian Current flows along this slope, varying the stratification in the horizontal, provides
462 lateral shears that can distort the internal tide response, and carrying eddies that can add
463 a strong time dependence to these effects. Even in two dimensions, the strength of the
464 internal tide reflection can be significantly impacted by the phase of the incoming tide with

465 other baroclinic modes Klymak et al. (2011) or the barotropic (Kelly and Nash 2010). The
466 simulations here exclude the local barotropic tide, so this would certainly complicate the
467 reflected response. Finally, the internal tide used here was monotonic, whereas the real tide
468 will also have other frequencies, most notably subinertial diurnal frequencies that will have
469 trapped wave responses (personal communication, R. Musgrave).

470 Regardless, it is useful to have studied the “simplest” response we could in this system
471 to tease apart the dominant physics. This response is complex, and it should be clear that
472 solely observational efforts to balance a reflection budget are going to be a challenge. Merging
473 simulations and observations is a likely way forward in understanding the wave field in this
474 complex slope region.

475 With respect to the reflection problem, the modeled slope has a relatively high reflection
476 back into the open ocean, with as much as 65% of the incoming energy being reflected as
477 mode-1. Its possible that higher resolution runs will be more dissipative, and that stronger
478 forcing will lead to a higher fraction of dissipation. However, these simulations, and the
479 results from the rest of the experiment to date (i.e. Johnston et al. 2015) indicate that bulk
480 of the energy from the Macquarie Ridge must dissipate elsewhere.

481 *Acknowledgments.*

482 Our thanks to conversations with Andy Dale on leaky slope waves and Qiang Li for
483 sharing his linear code for the Lindzen-Kuo method. J. Klymak was supported by the
484 Canadian National Science Engineering Research Council Discovery Grant 327920-2006, and
485 by computer time from the US Office of Naval Research, T. Palusziewicz, program officer.

⁴⁸⁶ H. Simmons and D. Brazhnikov were supported by NSF OCE 1130048. J. MacKinnon, and
⁴⁸⁷ R. Pinkel were supported by award NSF OCE 1129763. M. Alford was supported by NSF
⁴⁸⁸ OCE 1129246. A website for this paper with analysis scripts, intermediate data files, and
⁴⁸⁹ model setups is at <http://web.uvic.ca/~jklymak/ttide15>.

APPENDIX

492 Appendix Slope-wave calculation

493 The slope wave calculation follows the calculation made by Dale et al. (2001), where

494 there are more details. The linear equation for the pressure perturbations are assumed to

495 have form $P = p(x, z) \exp^{i(k_y y - \omega t)}$, where k_y is the along-slope wavenumber.

$$(f^2 - \omega^2) \frac{\partial}{\partial z} \left(\frac{\partial p / \partial z}{N^2 - \omega^2} \right) + \frac{\partial^2 p}{\partial x^2} - k_y^2 p = 0 \quad (\text{A1})$$

496 Subject to boundary conditions at the surface of $\partial p / \partial z = 0$ and at the sea floor of

$$\left(\frac{\omega^2 - f^2}{N^2 - \omega^2} \right) \frac{\partial p}{\partial z} = \frac{\partial h}{\partial x} \left(\frac{\partial p}{\partial x} - \frac{f k_y}{\omega} p \right) \quad (\text{A2})$$

497 The coast is assumed to be a wall, and the open ocean to consist of waves radiating away

498 from the slope, or if k_x , the cross-slope wavenumber, is imaginary, disturbances that decay

499 away from the slope.

500 The above are discretized on a domain that is 260 km wide into 261 grid cells in x ,

501 and onto a sigma-co-ordinate with 192 vertical levels. The hyperbolic method of solution

502 due to Lindzen and Kuo (1969) was used to solve on this domain for p for $\omega = 1.4f$,

503 $f = 10^{-4} \text{s}^{-1}$, and for a sweep of k_y . Under an arbitrary forcing certain values of k_y resonate

504 and lead to stronger amplitude responses in p corresponding to spatial modes of the system.

505 The numerical method is sensitive to the stratification, so we used a fit exponential of

506 $N^2(z) = 2 \times 10^{-5} \text{s}^{-2} e^{z/(1000 \text{ m})}$ (where z is negative downwards). The scan was taken over

507 300 wavelengths equally spaced between 30 and 180 km.

508 The resulting spatial modes are similar to those in Dale et al. (2001) (figure 16). There
509 is a peak of amplitude on the shelf, and then a second peak on the slope. As the slope gets
510 more narrow, the peak on the slope becomes broader. These shapes are the lowest modes.

511 The general code to solve this is at <https://github.com/jklymak/LindzenKuo>. The
512 code used for this paper is at <http://web.uvic.ca/~jklymak/ttide15/>.

REFERENCES

- 515 Baines, P. G., 2007: Internal tide generation by seamounts. *Deep Sea Res. I*, **54** (9), 1486 –
 516 1508, doi:10.1016/j.dsr.2007.05.009.
- 517 Bonod, N., E. Popov, and M. Nevière, 2005: Differential theory of diffraction by finite
 518 cylindrical objects. *JOSA A*, **22** (3), 481–490, doi:10.1364/JOSAA.22.000481.
- 519 Boyer, T., et al., 2013: *World Ocean Database 2013*. NOAA Atlas NESDIS 72, doi:10.7289/
 520 V5NZ85MT.
- 521 Buijsman, M. C., et al., 2014: Three-dimensional double-ridge internal tide resonance in
 522 Luzon Strait. *J. Phys. Oceanogr.*, **44** (3), 850–869, doi:10.1175/JPO-D-13-024.1.
- 523 Carter, G., et al., 2008: Energetics of M 2 Barotropic-to-Baroclinic Tidal Conversion at the
 524 Hawaiian Islands. *Journal of Physical Oceanography*, **38** (10), 2205–2223, doi:10.1175/
 525 2008JPO3860.1.
- 526 Dale, A. C., J. M. Huthnance, and T. J. Sherwin, 2001: Coastal-trapped waves and
 527 tides at near-inertial frequencies. *J. Phys. Oceanogr.*, **31** (10), 2958–2970, doi:10.1175/
 528 1520-0485(2001)031<2958:CTWATA>2.0.CO;2.
- 529 Dale, A. C. and T. J. Sherwin, 1996: The extension of baroclinic coastal-trapped wave
 530 theory to superinertial frequencies. *J. Phys. Oceanogr.*, **26** (11), 2305–2315, doi:10.1175/
 531 1520-0485(1996)026<2305:TEOBCT>2.0.CO;2.

- 532 Hall, R. A., J. M. Huthnance, and R. G. Williams, 2013: Internal wave reflection on shelf
533 slopes with depth-varying stratification. *J. Phys. Oceanogr.*, **43** (2), 248–258, doi:10.1175/
534 JPO-D-11-0192.1.
- 535 Hunter, J. D., 2007: Matplotlib: A 2D graphics environment. *Comput. Sci. Eng.*, **9** (3),
536 90–95, doi:10.1109/MCSE.2007.55.
- 537 Johnston, T. M. S., D. L. Rudnick, and S. M. Kelly, 2015: Standing internal tides in the Tas-
538 man Sea observed by gliders. *J. Phys. Oceanogr.*, **45** (11), doi:10.1175/JPO-D-15-0038.1.
- 539 Johnston, T. S. and M. A. Merrifield, 2003: Internal tide scattering at seamounts, ridges,
540 and islands. *J. Geophys. Res.*, **108** (C6), 3180, doi:10.1029/2002JC01528.
- 541 Kang, D., 2011: Barotropic and baroclinic tidal energy. Ph.D. thesis, Stanford University.
- 542 Kang, D. and O. Fringer, 2012: Energetics of barotropic and baroclinic tides in the Monterey
543 Bay area. *J. Phys. Oceanogr.*, **42** (2), 272–290, doi:10.1175/JPO-D-11-039.1.
- 544 Kelly, S. and J. Nash, 2010: Internal-tide generation and destruction by shoaling internal
545 tides. *Geophys. Res. Lett.*, **37**, L23 611, doi:10.1029/2010GL045598.
- 546 Kelly, S. M., N. L. Jones, and J. D. Nash, 2013a: A coupled model for Laplace's tidal
547 equations in a fluid with one horizontal dimension and variable depth. *J. Phys. Oceanogr.*,
548 doi:10.1175/JPO-D-12-0147.1.
- 549 Kelly, S. M., N. L. Jones, J. D. Nash, and A. F. Waterhouse, 2013b: The geography of
550 semidiurnal mode-1 internal-tide energy loss. *Geophys. Res. Lett.*, doi:10.1002/grl.50872.

- 551 Klymak, J., M. Alford, R. Pinkel, R. Lien, Y. Yang, and T. Tang, 2011: The breaking and
552 scattering of the internal tide on a continental slope. *J. Phys. Oceanogr.*, **41**, 926–945,
553 doi:10.1175/2010JPO4500.1.
- 554 Klymak, J. M. and S. M. Legg, 2010: A simple mixing scheme for models that resolve
555 breaking internal waves. *Ocean Modell.*, **33** (3-4), 224 – 234, doi:10.1016/j.ocemod.2010.
556 02.005.
- 557 Klymak, J. M., et al., 2006: An estimate of tidal energy lost to turbulence at the Hawaiian
558 Ridge. *J. Phys. Oceanogr.*, **36**, 1148–1164, doi:10.1175/JPO2885.1.
- 559 Legg, S. and J. M. Klymak, 2008: Internal hydraulic jumps and overturning generated by
560 tidal flow over a tall steep ridge. *J. Phys. Oceanogr.*, **38** (9), 1949–1964, doi:10.1175/
561 2008JPO3777.1.
- 562 Lindzen, R. and H.-L. Kuo, 1969: A reliable method for the numerical integration of a large
563 class of ordinary and partial differential equations. *Mon. Wea. Rev.*, **97** (10), 732–734,
564 doi:10.1175/1520-0493(1969)097<0732:ARMFTN>2.3.CO;2.
- 565 Marshall, J., A. Adcroft, C. Hill, L. Perelman, and C. Heisey, 1997: A finite-volume, incom-
566 pressible Navier-Stokes model for studies of the ocean on parallel computers. *J. Geophys.
567 Res.*, **102** (C3), 5753–5766, doi:10.1029/96JC02775.
- 568 Martini, K., M. Alford, J. Nash, E. Kunze, and M. Merrifield, 2007: Diagnosing a partly
569 standing internal wave in Mamala Bay, Oahu. *Geophys. Res. Lett.*, **34** (17), L17604,
570 doi:10.1029/2007GL029749.

- 571 Martini, K. I., M. H. Alford, E. Kunze, S. M. Kelly, and J. D. Nash, 2013: Internal bores and
572 breaking internal tides on the Oregon continental slope. *J. Phys. Oceanogr.*, **43**, 120–139,
573 doi:10.1175/JPO-D-12-030.1.
- 574 Melet, A., R. Hallberg, S. Legg, and K. Polzin, 2013: Sensitivity of the ocean state to the
575 vertical distribution of internal-tide-driven mixing. *J. Phys. Oceanogr.*, **43** (3), 602–615,
576 doi:10.1175/JPO-D-12-055.1.
- 577 Mercier, M. J., N. B. Garnier, and T. Dauxois, 2008: Reflection and diffraction of internal
578 waves analyzed with the Hilbert transform. *Phys. Fluids*, **20** (8), 086 601, doi:10.1063/1.
579 2963136.
- 580 Nash, J., M. Alford, E. Kunze, K. Martini, and S. Kelley, 2007: Hotspots of deep
581 ocean mixing on the Oregon continental slope. *Geophys. Res. Lett.*, **34**, L01 605,
582 doi:10.1029/2006GL028 170.
- 583 Nash, J. D., E. Kunze, J. M. Toole, and R. W. Schmitt, 2004: Internal tide reflection and
584 turbulent mixing on the Continental Slope. *J. Phys. Oceanogr.*, 1117–1134, doi:10.1175/
585 1520-0485(2004)034<1117:ITRATM>2.0.CO;2.
- 586 Polzin, K. L., 2009: An abyssal recipe. *Ocean Modelling*, **30** (4), 298–309, doi:10.1016/j.
587 ocemod.2009.07.007.
- 588 Rainville, L., T. Johnston, G. S. Carter, M. A. Merrifield, R. Pinkel, P. F. Worcester, and
589 B. D. Dushaw, 2010: Interference pattern and propagation of the M_2 internal tide south
590 of the Hawaiian Ridge. *J. Phys. Oceanogr.*, **40** (2), doi:10.1175/2009JPO4256.1.

- 591 Smith, W. and D. Sandwell, 1997: Global sea floor topography from satellite altimetry and
592 ship depth soundings. *Science*, **277** (5334), 1956, doi:10.1126/science.277.5334.1956.
- 593 St. Laurent, L. and C. Garrett, 2002: The role of internal tides in mixing the deep ocean. *J.*
594 *Phys. Oceanogr.*, **32**, 2882–2899, doi:10.1175/1520-0485(2002)032<2882:TROITI>2.0.CO;
595 2.
- 596 van der Walt, S., S. C. Colbert, and G. Varoquaux, 2011: The NumPy array: A structure
597 for efficient numerical computation. *Comput. Sci. Eng.*, **13** (2), 22–30, doi:10.1109/mcse.
598 2011.37.
- 599 Whiteway, T., 2009: Australian bathymetry and topography grid, june 2009. scale 1:5000000.
600 Tech. rep., Geoscience Australia, Canberra. doi:10.4225/25/53D99B6581B9A.
- 601 Zhao, Z. and M. H. Alford, 2009: New altimetric estimates of mode-1 M2 internal tides
602 in the central North Pacific Ocean. *J. Phys. Oceanogr.*, **39** (7), 1669–1684, doi:10.1175/
603 2009JPO3922.1.

604 List of Figures

- 605 1 Schematic of the difficulty of quantifying reflecting fluxes in an inhomogeneous
606 environment. Plane waves are trivial. Inhomogeneous incoming waves or
607 reflections are significantly more difficult. 38
- 608 2 Location of TTide experiment: a) Energy flux in a regional numerical sim-
609 ulation. Color is the absolute value of the flux, arrows it's direction. The
610 magenta box indicates the numerical modeling domain used in this paper. b)
611 Detail of the bathymetry on the Tasman slope. The magenta lines indicate
612 100 km in the x-direction, and 300 km in the y direction in the modeling
613 domain used in this paper. 39
- 614 3 a) Forcing used to drive the models used in this paper. Two mode-1 internal
615 wave sources are located to the south east (blue lines). The model domain
616 is rotated 12 degrees from geographic so the shelf break approximately lies
617 along $x = 0$. Typical model domain and sponge region is indicated as green
618 rectangles. The 250, and 3000-m isobaths are contoured. Arrows show the
619 direction of the energy flux, and are scaled by its strength. b) Energy flux of
620 analytical response of energy reflecting from a wall at $x = 0$, north of $y = 0$.
621 c) Phase of reflected response. 40

622 4 a)–d) Surface x-direction velocity for four snapshots. a) is the initial condi-
623 tions (slightly modified after a tidal cycle) and d) is the steady state. Grey
624 contours are depths at 3000, 2000, 1000, and 250-m. e)–h) is depth-integrated
625 baroclinic energy flux at the same time periods, with arrows indicating direc-
626 tion.

41

627 5 Energy budget over the 19th tidal cycle of a) Barotropic to baroclinic con-
628 version; b) Baroclinic energy flux convergence ($-\nabla F_{bc}$); c) rate of change
629 of baroclinic energy; d) residual representing the dissipation in the model
630 $D = -\nabla F_{bc} + \text{Conv.} - dE/dt$. The green box is the region for the energy time
631 series (figure 6b).

42

6 a) Integral in x to 80 km offshore of the energy terms in figure 5 for the
REAL case. Note that the barotropic-baroclinic term (red) is of the same
order as the baroclinic convergence (cyan) and the residual dissipation (gray)
for most of the slope. b) Energy budget time series for the “Real” case,
tidally averaged, where time is normalized by $T = 12.4h$, between $y = 0$ to
 $y = 400$ km. There is still a small residual increase in the energy with time
(purple), representing the accumulation of high-mode energy in the region.
Net barotropic-baroclinic conversion (red) is small and negative, indicating a
small net loss to the barotropic tide in this region. The bulk of the budget
is the balance between baroclinic flux convergence (blue) and the residual
“dissipation” (gray). c) Net flux in the box defined by $0 < x < 80$ km, and
 $0 < y < 400$ km. Green is the value for the net flux (no modal decomposition).
Blue bars are the modal decomposition. There is a net incoming flux in mode
1 and net reflecting fluxes in higher modes (primarily modes 2-4).

645 43
646 7 Cross sections of topographies from $y = 50$ km. 44

647 8 Energy flux for six geometries at tidal cycle 20. Grey depth contours are
648 -3000, -2000, -1000 and -250 m. Arrows indicate the direction of energy flux.

649 See figure 7 for bathymetry cross sections at $y = 50$ km. 45

- 650 9 Mode-1 decomposition of energy fluxes for the SHELF experiment. a) Incoming
 651 energy flux calculated from the NO TOPO simulation (figure 8a). Note
 652 that the shelf bathymetry is contoured on this plot (grey lines, and green
 653 “land”), but this bathymetry was not part of this simulation. The green
 654 line demarks the region the energy budget in the inset was integrated over.
 655 The green diamonds are the location of a synthetic mooring, and the arrow
 656 indicates the estimated incoming flux from a plane wave fit over the three
 657 moorings of the “Total” simulation (see text). b) Reflected energy flux cal-
 658 culated from the difference between the velocities and displacements of the
 659 Total simulation (panel d) and the “Incoming” (panel a). Blue arrow is the
 660 outgoing flux from a plane wave fit over the mooring array from the “Total”
 661 simulation. c) Energy flux cross terms between the incoming and outgoing
 662 waves. d) Total simulation from the SHELF case (figure 8d) 46
- 663 10 Energy partition as in figure 9, taking the ROUND RISE simulation as the
 664 incoming wave, and SHELF/RISE simulation as the total wavefield. 47
- 665 11 Energy partition as in figure 9, taking the RISE simulation as the incoming
 666 wave, and REAL simulation as the total wavefield. 48

- 667 12 a) Energy budget from 80 km by 80 km control volumes along the continental
 668 slope from the REAL simulations. The incoming flux (red) is compared to the
 669 reflected (blue) and the cross terms (purple). b) The reflection co-efficients.
 670 The blue line is R_1 , the mode-1 reflectivity in the 80-km control volumes along
 671 slope from the non-linear simulation. The black line is the mode-1 reflectivity
 672 from a linear model (Kelly et al. 2013a), and the grey lines behind are the
 673 cumulative sum of modes 2, to 5 and then all the modes. These do not sum
 674 up to one because the linear model has some “viscosity” that removes some
 675 high-mode energy. The dashed lines are the mean of R_1 from the linear model
 676 if a constant average is taken (light blue, dashed), and if weighted by the
 677 diffracted beam strength (purple, dashed). 49
- 678 13 Barotropic to baroclinic conversion for different shelf widths from widest (a)
 679 to narrowest (d). Arrows are barotropic flux vectors. Note how the along-
 680 slope barotropic flux is almost entirely confined to conversion dipoles along
 681 slope. 50
- 682 14 Along-slope spectra of across slope velocity (thick lines) for the three narrow-
 683 est slopes in figure 13, from velocities on the shallow shelf in these simulations.
 684 The thin lines are resonance curves, formed from the cross-slope equations of
 685 motion assuming harmonic motion in time and along-slope. As along-slope
 686 wavenumber is varied resonant modes have a stronger response. What is
 687 plotted is arbitrary units for the three slope geometries. 51

- 688 15 Terms from the energy budget for 40-km wide slope. The incoming and re-
689 flected energy fluxes are computed at $x = 40$ km, and the conversion term
690 integrated from the shelf to $x = 40$ km. 52
- 691 16 Spatial shape of modes picked out from the resonant searching technique (as
692 shown in figure 14) for the 70, 40 and 20-km wide slopes. 53

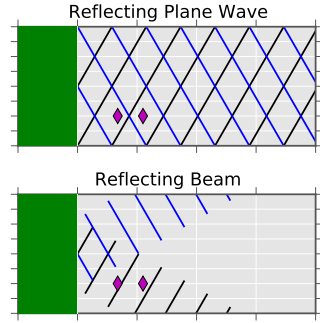


FIG. 1. Schematic of the difficulty of quantifying reflecting fluxes in an inhomogeneous environment. Plane waves are trivial. Inhomogeneous incoming waves or reflections are significantly more difficult.

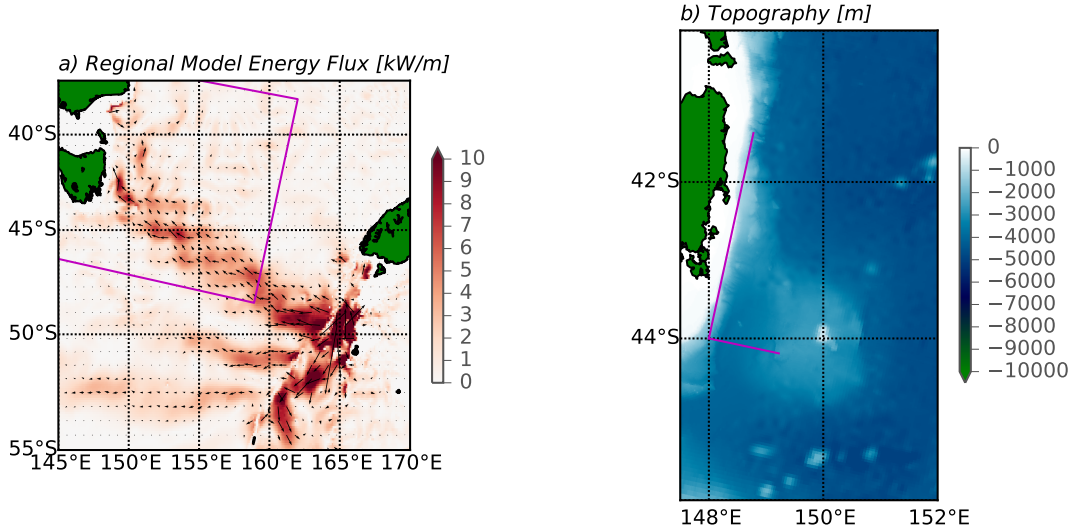


FIG. 2. Location of TTide experiment: a) Energy flux in a regional numerical simulation. Color is the absolute value of the flux, arrows its direction. The magenta box indicates the numerical modeling domain used in this paper. b) Detail of the bathymetry on the Tasman slope. The magenta lines indicate 100 km in the x-direction, and 300 km in the y direction in the modeling domain used in this paper.

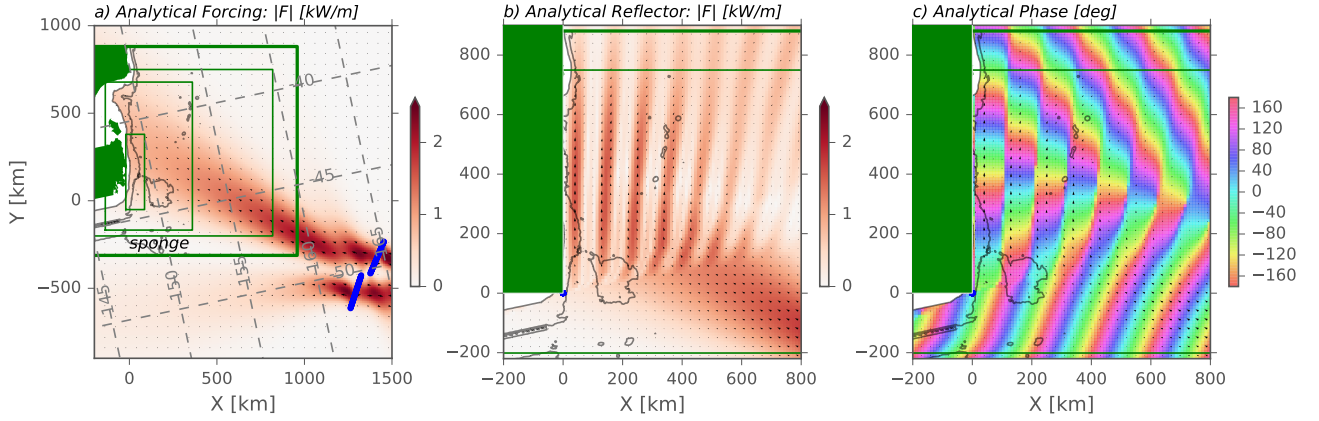


FIG. 3. a) Forcing used to drive the models used in this paper. Two mode-1 internal wave sources are located to the south east (blue lines). The model domain is rotated 12 degrees from geographic so the shelf break approximately lies along $x = 0$. Typical model domain and sponge region is indicated as green rectangles. The 250, and 3000-m isobaths are contoured. Arrows show the direction of the energy flux, and are scaled by its strength. b) Energy flux of analytical response of energy reflecting from a wall at $x = 0$, north of $y = 0$. c) Phase of reflected response.

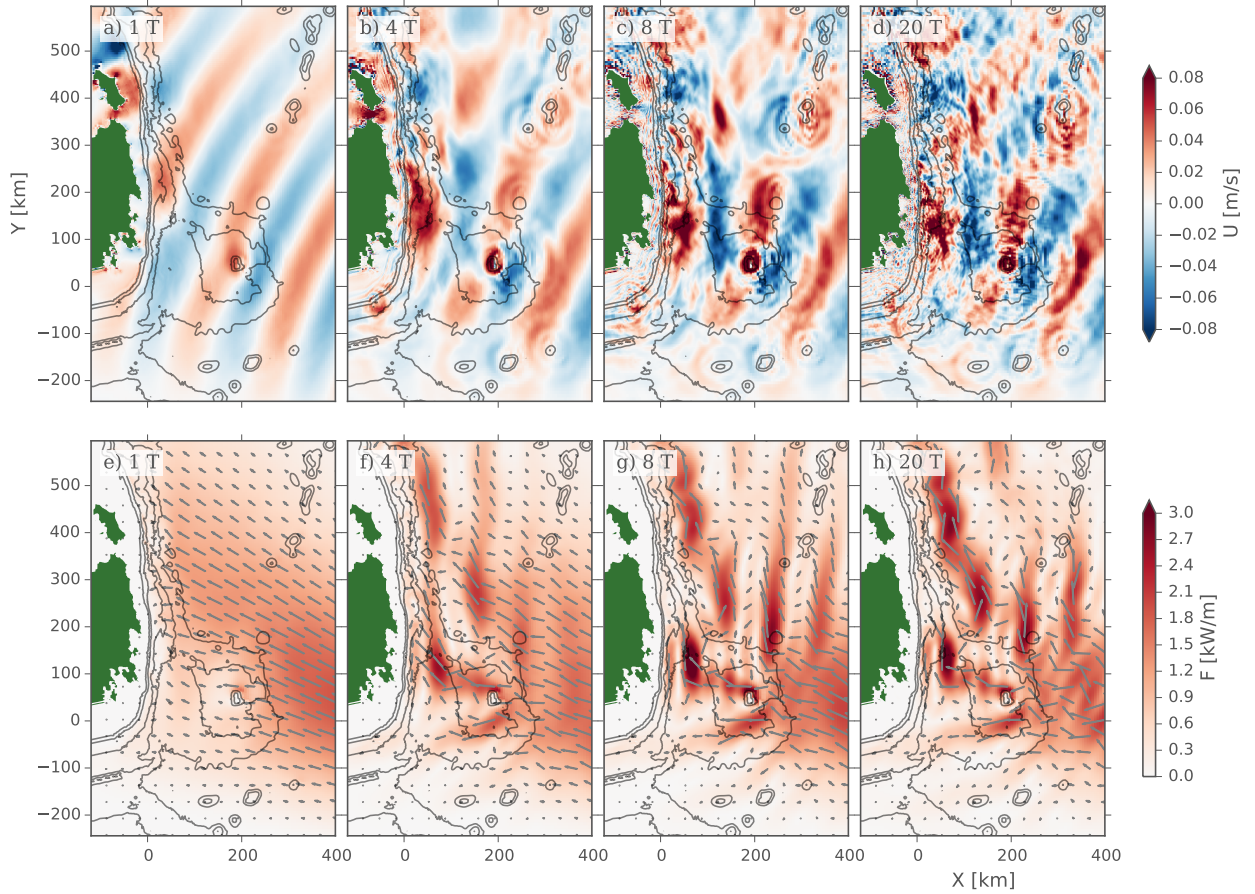


FIG. 4. a)–d) Surface x-direction velocity for four snapshots. a) is the initial conditions (slightly modified after a tidal cycle) and d) is the steady state. Grey contours are depths at 3000, 2000, 1000, and 250-m. e)–h) is depth-integrated baroclinic energy flux at the same time periods, with arrows indicating direction.

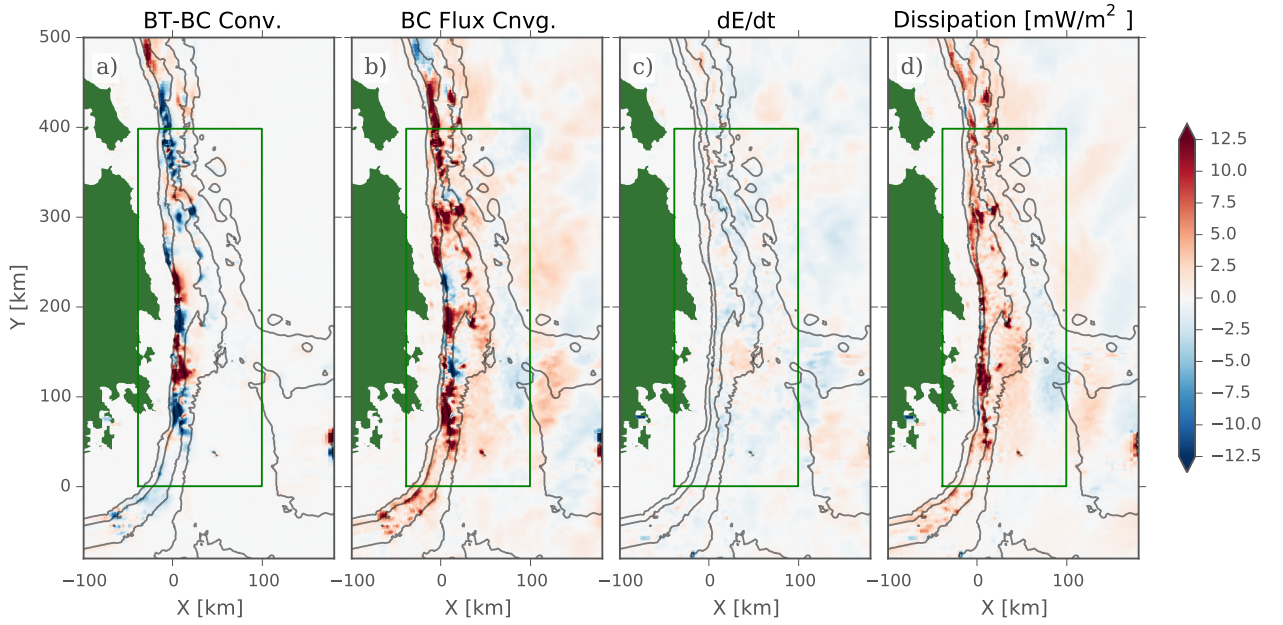


FIG. 5. Energy budget over the 19th tidal cycle of a) Barotropic to baroclinic conversion; b) Baroclinic energy flux convergence ($-\nabla F_{bc}$); c) rate of change of baroclinic energy; d) residual representing the dissipation in the model $D = -\nabla F_{bc} + \text{Conv.} - dE/dt$. The green box is the region for the energy time series (FIG. 6b).

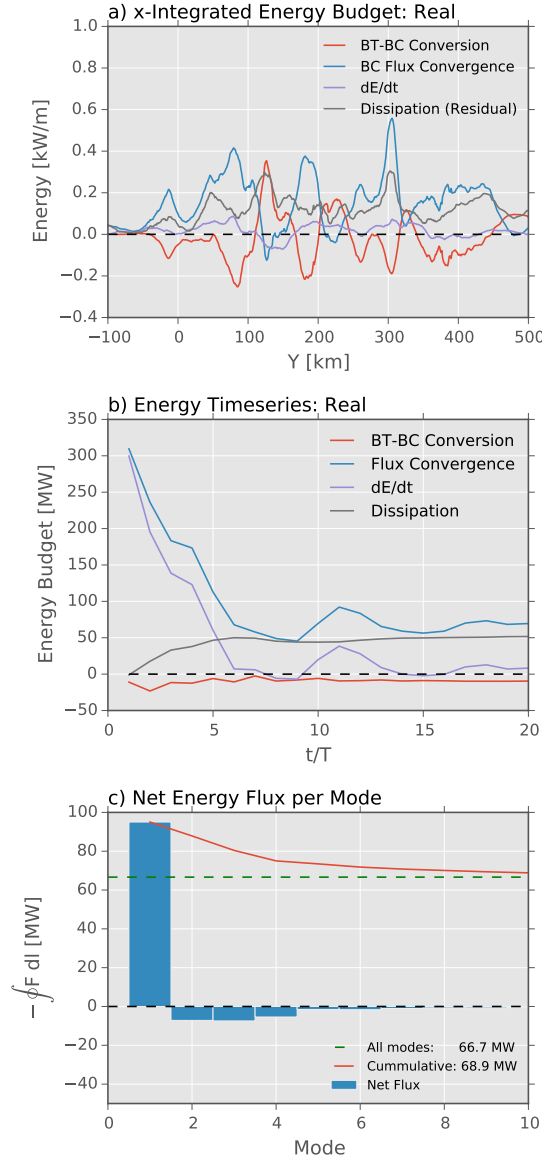


FIG. 6. a) Integral in x to 80 km offshore of the energy terms in FIG. 5 for the REAL case. Note that the barotropic-baroclinic term (red) is of the same order as the baroclinic convergence (cyan) and the residual dissipation (gray) for most of the slope. b) Energy budget time series for the “Real” case, tidally averaged, where time is normalized by $T = 12.4h$, between $y = 0$ to $y = 400$ km. There is still a small residual increase in the energy with time (purple), representing the accumulation of high-mode energy in the region. Net barotropic-baroclinic conversion (red) is small and negative, indicating a small net loss to the barotropic tide in this region. The bulk of the budget is the balance between baroclinic flux convergence (blue) and the residual “dissipation” (gray). c) Net flux in the box defined by $0 < x < 80$ km, and $0 < y < 400$ km. Green is the value for the net flux (no modal decomposition). Blue bars are the modal decomposition. There is a net incoming flux in mode 1 and net reflecting fluxes in higher modes (primarily modes 2-4).

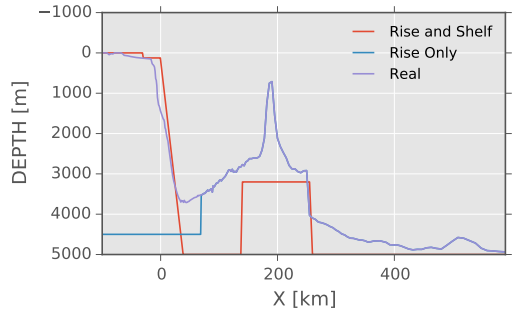


FIG. 7. Cross sections of topographies from $y = 50$ km.

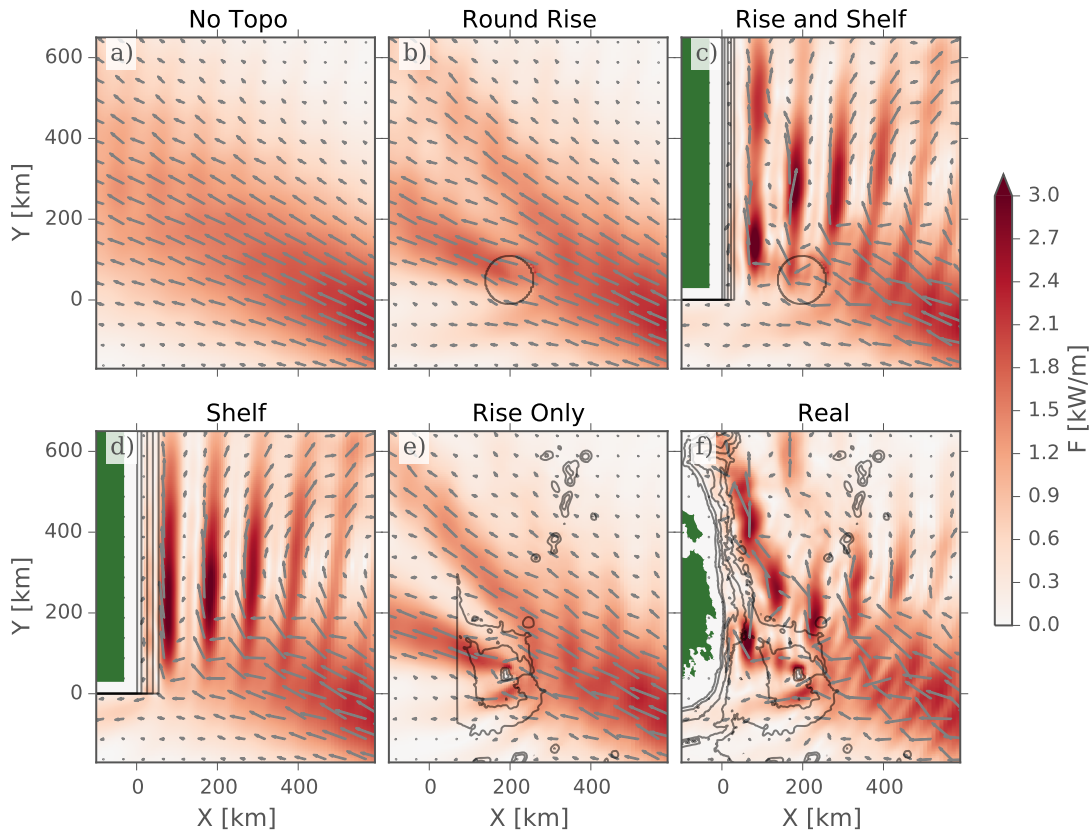


FIG. 8. Energy flux for six geometries at tidal cycle 20. Grey depth contours are -3000, -2000, -1000 and -250 m. Arrows indicate the direction of energy flux. See FIG. 7 for bathymetry cross sections at $y = 50$ km.

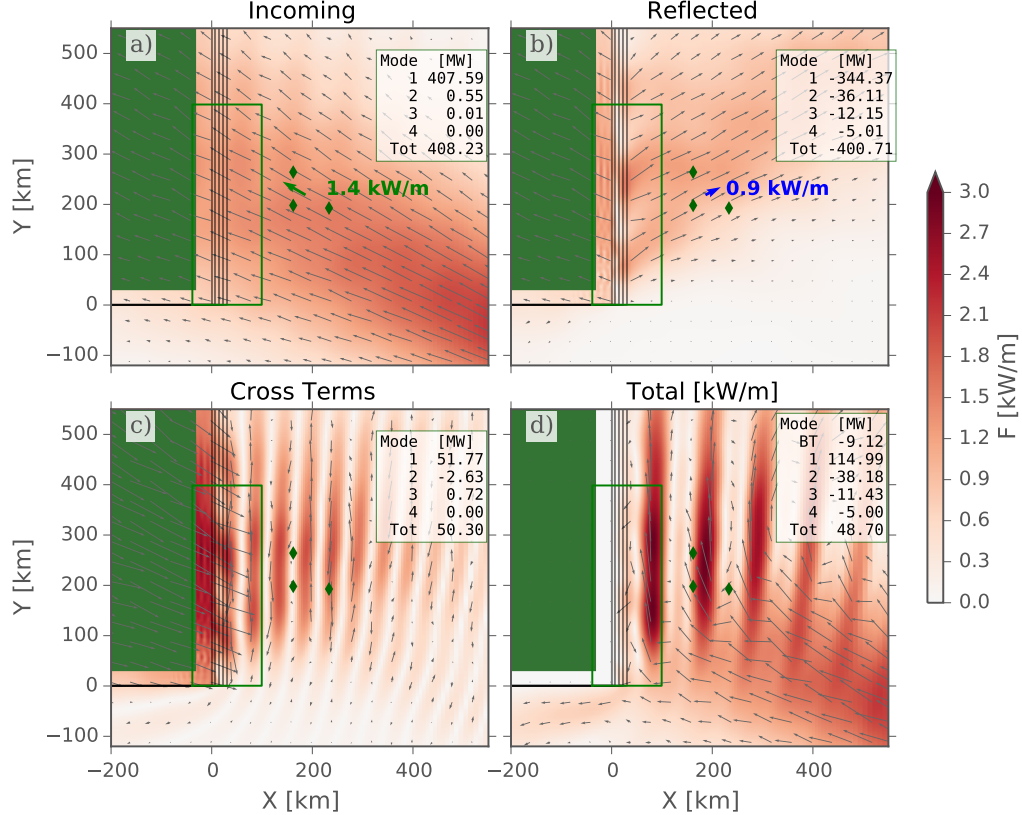


FIG. 9. Mode-1 decomposition of energy fluxes for the SHELF experiment. a) Incoming energy flux calculated from the NO TOPO simulation (FIG. 8a). Note that the shelf bathymetry is contoured on this plot (grey lines, and green “land”), but this bathymetry was not part of this simulation. The green line demarks the region the energy budget in the inset was integrated over. The green diamonds are the location of a synthetic mooring, and the arrow indicates the estimated incoming flux from a plane wave fit over the three moorings of the “Total” simulation (see text). b) Reflected energy flux calculated from the difference between the velocities and displacements of the Total simulation (panel d) and the “Incoming” (panel a). Blue arrow is the outgoing flux from a plane wave fit over the mooring array from the “Total” simulation. c) Energy flux cross terms between the incoming and outgoing waves. d) Total simulation from the SHELF case (FIG. 8d)

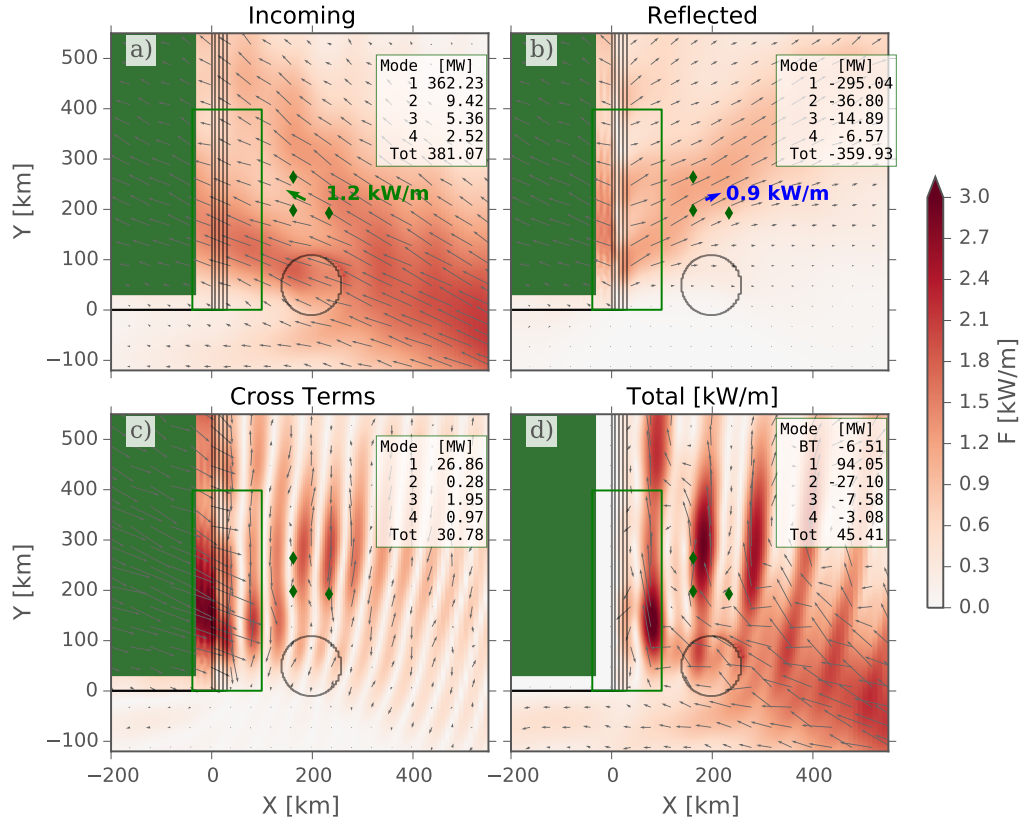


FIG. 10. Energy partition as in FIG. 9, taking the ROUND RISE simulation as the incoming wave, and SHELF/RIZE simulation as the total wavefield.

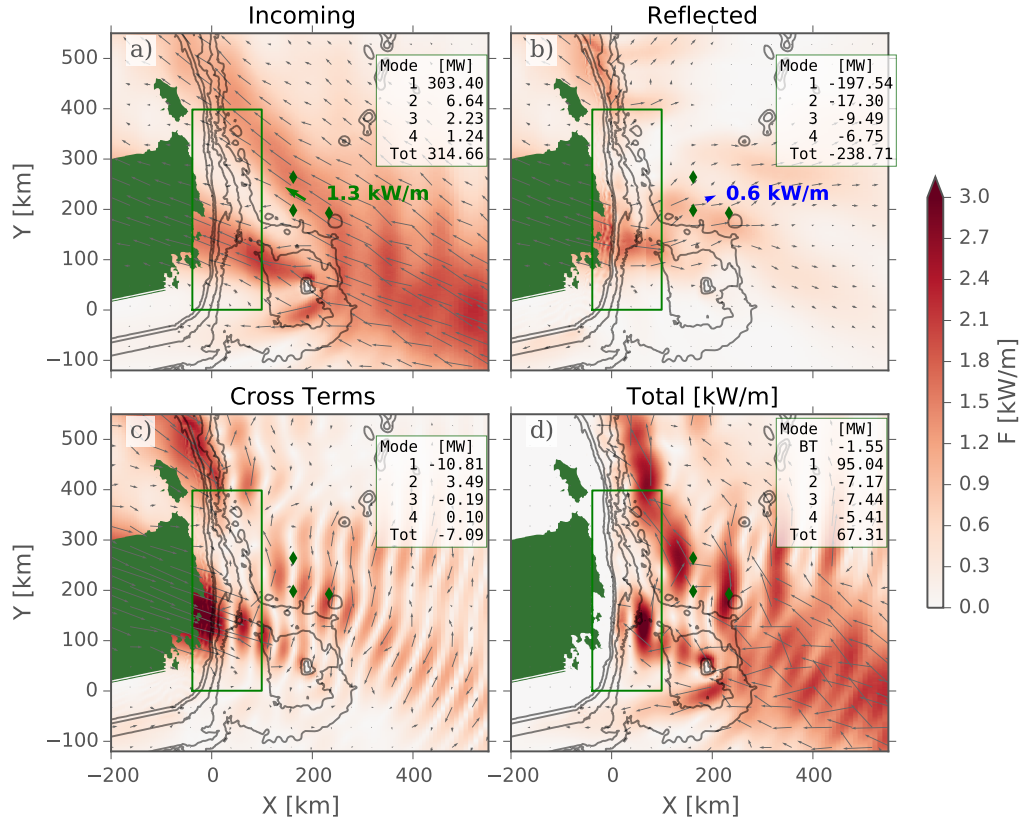


FIG. 11. Energy partition as in FIG. 9, taking the RISE simulation as the incoming wave, and REAL simulation as the total wavefield.

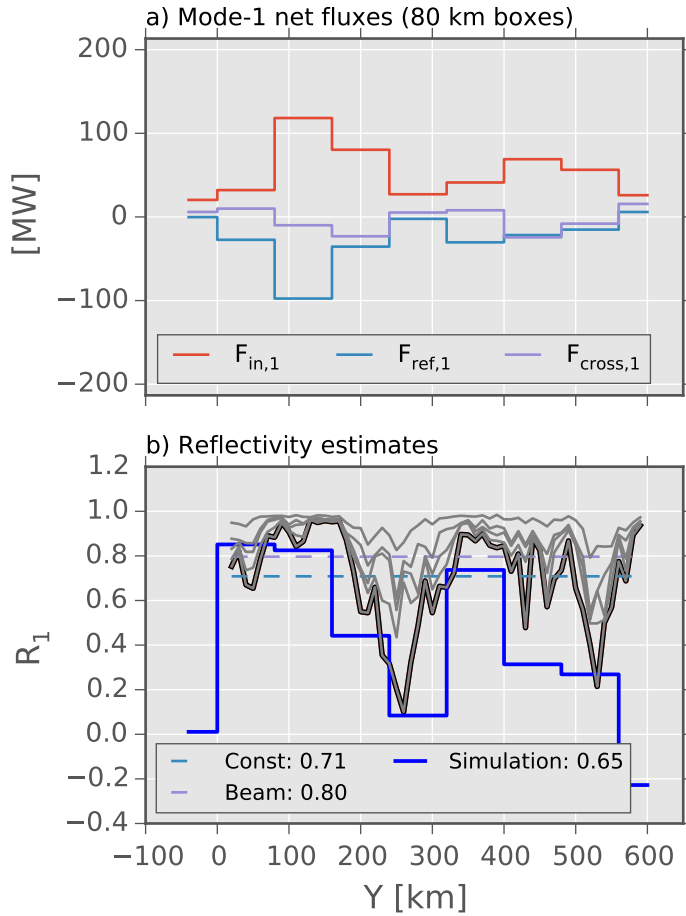


FIG. 12. a) Energy budget from 80 km by 80 km control volumes along the continental slope from the REAL simulations. The incoming flux (red) is compared to the reflected (blue) and the cross terms (purple). b) The reflection co-efficients. The blue line is R_1 , the mode-1 reflectivity in the 80-km control volumes along slope from the non-linear simulation. The black line is the mode-1 reflectivity from a linear model (Kelly et al. 2013a), and the grey lines behind are the cumulative sum of modes 2, to 5 and then all the modes. These do not sum up to one because the linear model has some “viscosity” that removes some high-mode energy. The dashed lines are the mean of R_1 from the linear model if a constant average is taken (light blue, dashed), and if weighted by the diffracted beam strength (purple, dashed).

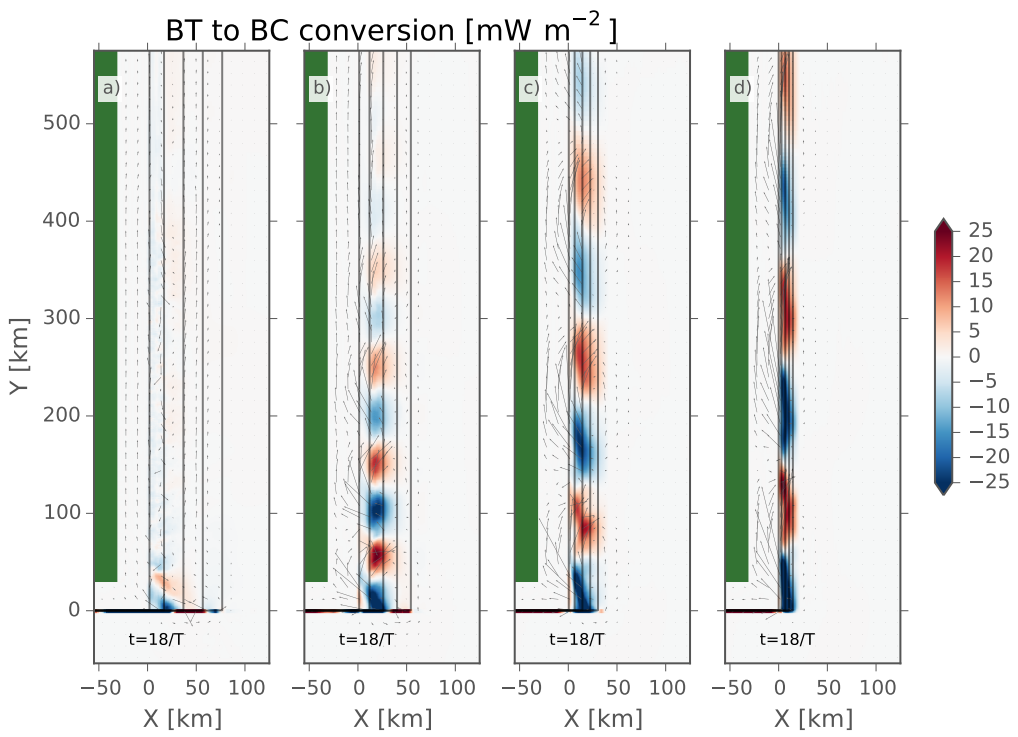


FIG. 13. Barotropic to baroclinic conversion for different shelf widths from widest (a) to narrowest (d). Arrows are barotropic flux vectors. Note how the along-slope barotropic flux is almost entirely confined to conversion dipoles along slope.

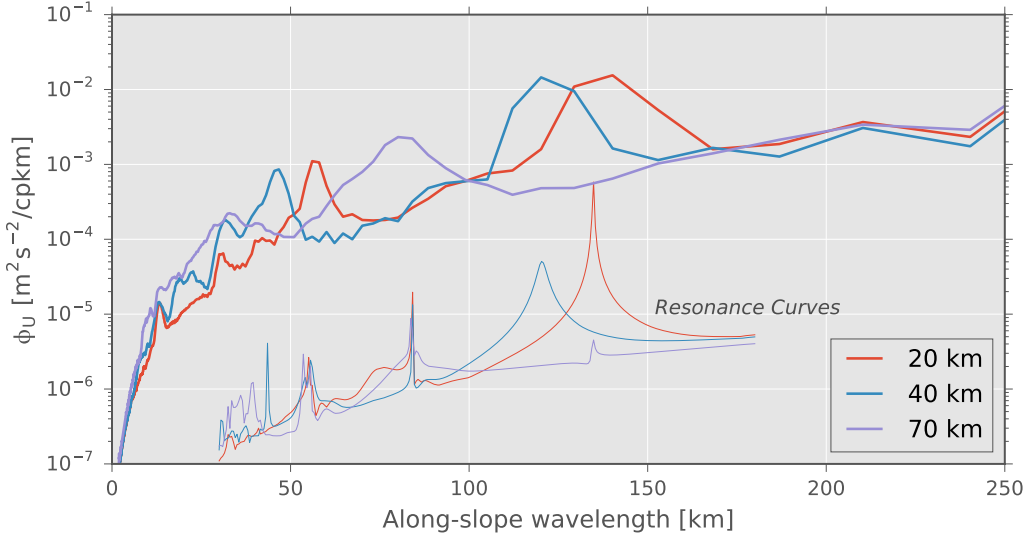


FIG. 14. Along-slope spectra of across slope velocity (thick lines) for the three narrowest slopes in FIG. 13, from velocities on the shallow shelf in these simulations. The thin lines are resonance curves, formed from the cross-slope equations of motion assuming harmonic motion in time and along-slope. As along-slope wavenumber is varied resonant modes have a stronger response. What is plotted is arbitrary units for the three slope geometries.

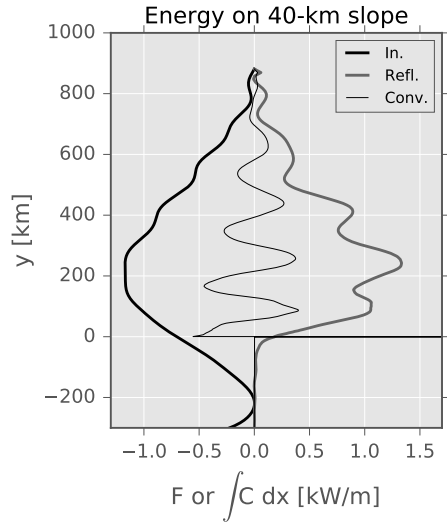


FIG. 15. Terms from the energy budget for 40-km wide slope. The incoming and reflected energy fluxes are computed at $x = 40$ km, and the conversion term integrated from the shelf to $x = 40$ km.

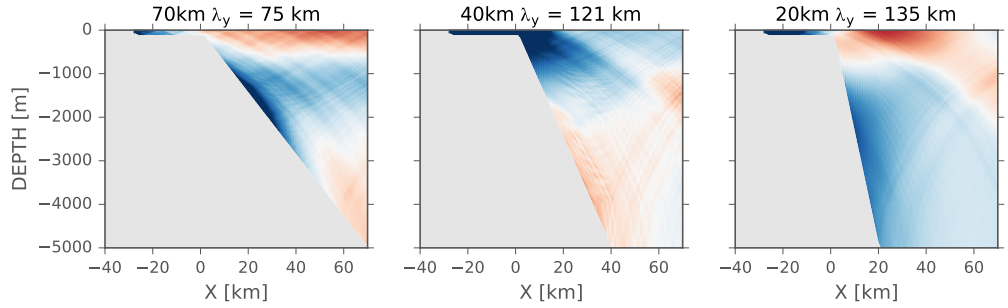


FIG. 16. Spatial shape of modes picked out from the resonant searching technique (as shown in FIG. 14) for the 70, 40 and 20-km wide slopes.